Implosion Dynamics in Direct-Drive Experiments

Introduction

Direct-drive inertial confinement fusion uses laser beams to implode a spherical shell.[1] The laser energy is absorbed near the critical surface of the target, transferred through the conduction zone to the ablation region, and converted into the kinetic energy of the shell through the rocket effect. Near peak compression, a fraction of the kinetic energy of the imploding shell is converted to the internal energy of the fuel. When the ion temperature of the central region (hot spot) and the areal density of the compressed fuel are sufficiently large, a burn wave originating from the alpha particles produced by the fusion of deuterium (D) and tritium (T) will propagate through the confined fuel in the shell (ignition).

The OMEGA Laser System[2] is used to study the physics of direct-drive fusion and could demonstrate a hydrodynamically equivalent implosion that, when scaled to the available energy at the National Ignition Facility (NIF, 1.5 MJ), would produce ignition.[3,4] One-dimensional (1-D) hydrodynamic simulations performed using the code *LILAC*,[5] including nonlocal thermal conduction[6] and cross-beam energy transfer (CBET) models,[7,8] show that a hydrodynamically equivalent ignition design on OMEGA requires a final implosion velocity $V_{imp} > 3.5 \times 10^7$ cm/s, an areal density $\rho R > 300$ mg/cm^2, and a final hot-spot pressure $P_{hs} > 100$ Gbar (Ref. 9). To achieve these conditions with the current ablation pressure on OMEGA, a target design with an in-flight aspect ratio (IFAR) of 30 is required, where the IFAR is a measure of the hydrodynamic stability of the implosion[10] given by the ratio of the radius to the thickness of the shell at a convergence ratio of 1.5 (Fig. 139.5).

An extensive set of experiments on OMEGA has been used to study the implosion performance in targets made of an outer layer of deuterated plastic (CD) and an inner layer of cryogenic DT ice surrounding DT gas.[9,11] In these experiments, a threshold was characterized in the shell adiabat and IFAR space, where below the IFAR threshold, the areal density calculated in 1-D simulations is recovered in the experiments. Simulations showed that a hydro-equivalent ignition design on OMEGA is above the threshold (Fig. 139.5).

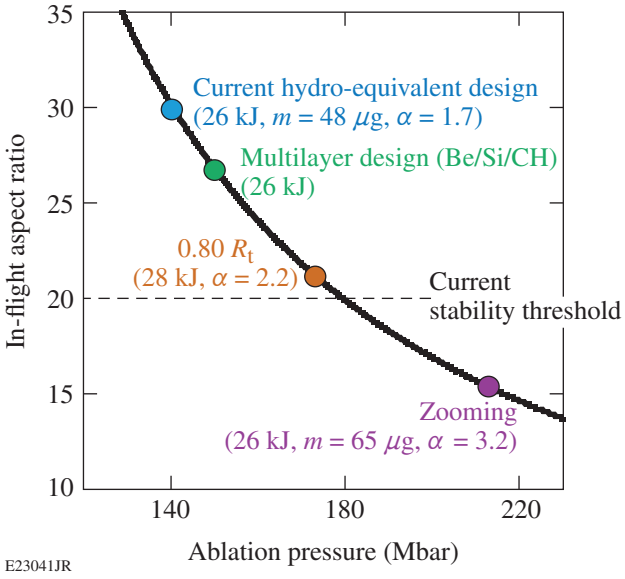

Figure 139.5
In-flight aspect ratio calculated at a convergence ratio of 1.5 as a function of ablation pressure (black curve) calculated at the end of the laser pulse for OMEGA direct-drive designs where the areal density (ρR = 300 mg/cm^2), implosion velocity ($V_{imp} = 3.7 \times 10^7$ cm/s), and hot-spot pressure (P_{hs} = 180 Mbar) are held constant. The designs used triple-picket laser pulses with a maximum intensity of 9×10^{14} W/cm^2. Simulations for the current cryogenic configuration (blue circle), a multilayer configuration (green circle), a configuration with a 20%-reduced beam size (orange circle), and a zooming configuration (purple circle) are shown. The current experimental stability threshold is indicated (dashed line).

Figure 139.5 shows a 1-D design curve generated by increasing the ablation pressure while maintaining a constant areal density (ρR = 300 mg/cm^2), implosion velocity ($V_{imp} = 3.7 \times 10^7$ cm/s), and hot-spot pressure (P_{hs} = 180 Gbar). Increasing the ablation pressure leads to a more-stable design (lower IFAR); when using higher ablation pressure, a thicker shell and larger adiabat can be used to maintain a constant implosion velocity, areal density, and hot-spot pressure. Figure 139.5 illustrates that increasing the ablation pressure from 140 Mbar (current design) to 180 Mbar is likely to achieve ignition hydro-equivalent implosions on OMEGA, assuming the current level of target nonuniformity seeds.

In this article, the transfer of laser energy to the kinetic energy of the shell (hydrodynamic efficiency) is studied for three different direct-drive–implosion experiments: cryogenic experiments,[11] ablator material experiments,[12] and reduced-beam-size experiments.[13] Experimental measurements of both the laser absorption and the implosion velocity are compared with 1-D hydrodynamic simulations. In each case, excellent agreement is observed, indicating that the simulations accurately reproduce the hydrodynamic efficiency. Simulations showed that an ~10% increase in the ablation pressure was obtained for a Be ablator compared with a CH ablator. When the radius of the laser beams was reduced by 50%, nearly all of the ablation pressure lost to CBET was recovered and the ablation pressure was increased by ~60%.

Results

The experiments discussed here were conducted on the OMEGA laser, where sixty 351-nm laser beams illuminated spherical shells. The hydrodynamic coupling was studied in cryogenic experiments, ablator material experiments, and reduced-beam-size experiments. In each case, the scattered-light power was measured to determine the absorption, while the shell trajectory, velocity, and neutron bang time were measured to quantify the transfer of the absorbed energy into the shell's kinetic energy. The experimental observables were compared with hydrodynamic simulations performed using the code *LILAC*,[5] which includes nonlocal thermal transport[6] and CBET[8] models. The simulated trajectories were obtained by post-processing the 1-D hydrodynamic parameters with *Spect3D*[14] to determine synthetic self-emission images. The simulations were used to determine the ablation pressure for the various cases and to assess the potential improvements in ignition hydro-equivalent OMEGA designs.

1. Cryogenic Experiments

The total laser energy in the cryogenic experiment was 26.6 kJ. The laser beams were smoothed by polarization smoothing (PS),[15] smoothing by spectral dispersion (SSD),[16] and distributed phase plates [SG4-DPP, fourth-order super-Gaussian with a 650-μm full width at half maximum (FWHM)].[17] A laser pulse with three short pickets was used to set the implosion target on a moderate adiabat (α = 3.7) (Ref. 18), followed by a 1.2-ns square pulse that accelerated a shell with an initial radius of 435 μm. The shell was made with a 7.4-μm CD ablator on top of a 52.2-μm-thick cryogenic DT ice layer.

The total unabsorbed laser energy was measured by five calorimeters located around the target chamber with an uncertainty of 5%. The scattered-light power was measured at four locations by multiplexing the signal into a 1.5-m spectrometer with a high-dynamic-range streak camera. The system had a 100-ps (FWHM) temporal resolution.

Figure 139.6 compares the measured and simulated time-resolved unabsorbed laser light. The excellent agreement between them indicates that the CBET model accurately reproduces the laser power absorbed in the plasma; the simulation also shows that nearly half of the scattered light is a result of CBET. The small discrepancy observed around 1.6 ns could be caused by an error in the CBET calculation during the rise of the laser pulse, where the hydrodynamic conditions evolve rapidly.

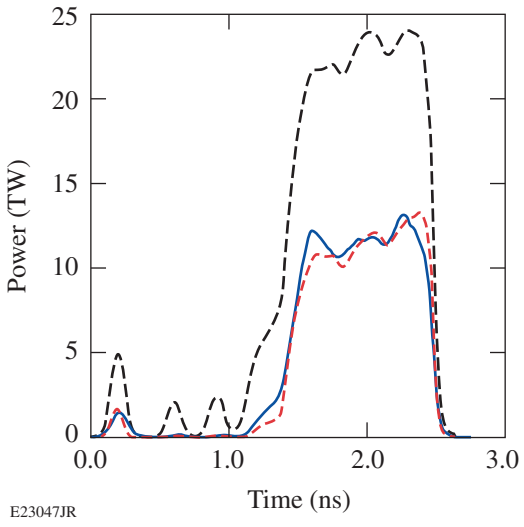

Figure 139.6
Comparison of the calculated (red dashed line) and measured (blue solid line) scattered-light power. The laser pulse is plotted (black dashed line).

Figure 139.7 shows excellent agreement between the measured and simulated shell trajectories. These results suggest that the nonlocal transport model accurately calculates this coupling since the transfer of the absorbed laser energy to the shell motion depends primarily on the thermal transport. A small discrepancy was obtained in the ablation-front position at early times when the simulated radius was ~10 μm smaller than the measured radius. The early discrepancy may be explained by the small difference in laser absorption measured during the rise of the main pulse.

The agreement observed between the simulated and measured shell trajectory is consistent with the good agreement observed in the time of neutron production (Fig. 139.7). The total

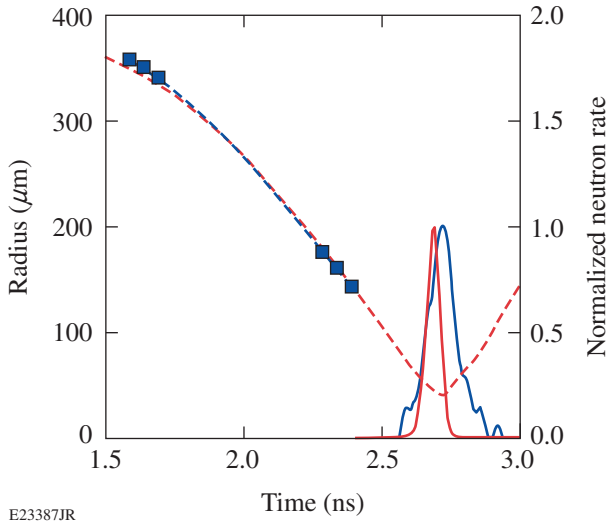

Figure 139.7
Comparison of the calculated (red dashed line) and measured (squares) shell trajectory and calculated (red solid line) and measured (blue solid line) normalized neutron-production rates obtained for the current cryogenic design. The third-order polynomial fit to the experimental data is shown (blue dashed line).

neutron production was 5× lower in the experiment than in simulation (the neutron production is normalized in Fig. 139.7), likely related to shell perturbations that compromise the implosion.

The self-emission shadowgraphy technique[19] was used to determine the shell trajectories. The soft x rays emitted by the imploding target were integrated over 40 ps and imaged with an array of pinholes onto a four-strip fast x-ray framing camera (XRFC).[20] The distinct peak in the emission-profile images resulted from the high density and temperature at the ablation surface and the large integration distance for the emission that reaches the XRFC (limb effect). In the cryogenic target experiments,[9] the primarily DT shell is optically thin to the CD emission at early times [Figs. 139.8(a) and 139.8(b)] and the ablation front is determined from the peak of the emission.[21] At late times [Figs. 139.8(e) and 139.8(f)], the shell is optically thick to the DT emission and the ablation front is determined from the position of the inner gradient. During the transition time when the CD is being ablated [Figs. 139.8(c) and 139.8(d)], the CD emission peak separates from the ablation surface and cannot be used to determine the ablation-front position. During this time, the ablation-front trajectory is inferred by fitting the

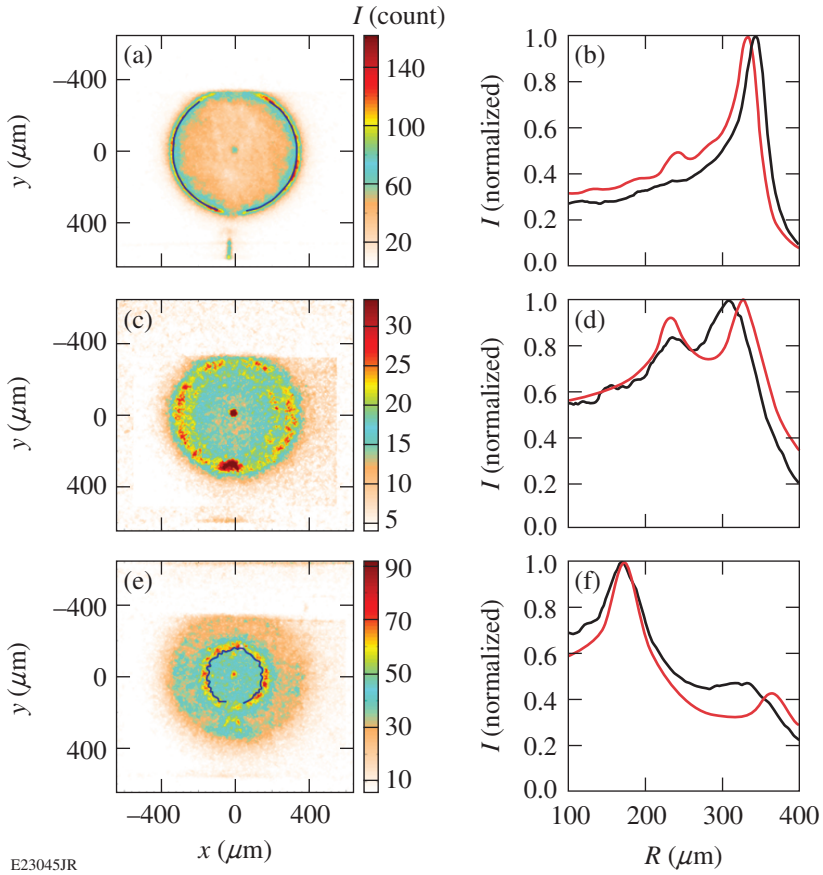

Figure 139.8
[(a),(c),(e)] Self-emission x-ray images from a cryogenic experiment; [(b),(d),(f)] comparison of the lineouts averaged over the entire experimental image (black line) with lineouts calculated from the simulations (red line) at [(a),(b)] t = 1680 ps, [(c),(d)] t = 2145 ps, and [(e),(f)] t = 2325 ps.

ablation-front position measured at early and late times with a third-order polynomial. A standard deviation of the peak (inner gradient) location around the image of $\sigma_{abl} = 2\ \mu$m ($\sigma_{abl} = 5\ \mu$m) is obtained. These positions are averaged as $N = 2\pi/\theta_{av} \sim 60$ independent measurements (where each lineout is averaged over $\theta_{av} = 5°$) to give a resulting accuracy for the averaged radius of $\sigma_{abl}/\sqrt{N} < 1\ \mu$m (Ref. 21).

The shell radii measured on two consecutive XRFC strips, 200 ps apart, were used to calculate time-averaged shell velocities. The relative timing between the XRFC strips was known to within 5 ps and the absolute timing to the laser pulse to within 30 ps (Ref. 12). The accuracy in the velocity (dV/V) was ~4% for a shell velocity of 200 km/s, given by

$$\frac{dV}{V} = \left[\frac{d(\Delta R)}{\Delta R} + \frac{d(\Delta t)}{\Delta t}\right]^{1/2},$$

where the error in the radius was $d(\Delta R)/\Delta R = 0.7/40\ \mu\text{m} = 1.8\%$ and the error in the timing was $d(\Delta t)/\Delta t = 7/200$ ps = 3.5%.

2. Ablator Material Experiments

In the ablator experiments, the overlapped intensity was varied by changing the total energy on target from 18.5 kJ (low intensity, $I = 4.5 \times 10^{14}$ W/cm^2) to 23 kJ (high intensity, $I = 7.2 \times 10^{14}$ W/cm^2). The laser beams were smoothed by PS, SSD, and SG4-DPP. Three 100-ps-long pickets were used to set the target implosion onto a low adiabat followed by a 1.2-ns (high-intensity) and 1.6-ns (low-intensity) square pulse that drove the target to its final velocity. The three ablators had mass densities of 1.03 g/cm^3 (CH), 3.35 g/cm^3 (C), and 1.83 g/cm^3 (Be). Their thicknesses were varied to maintain the initial total ablator mass to be equivalent to a 27-μm-thick CH shell. The outer radius at low energy and at high energy was 440 μm and 445 μm, respectively, and the total mass was 62±1 μg and 64±2 μg, respectively.

Figure 139.9 shows the simulated and measured shell trajectories and scattered powers for three different ablator materials: beryllium $(\text{Be}, \langle A\rangle/\langle Z\rangle = 2.25)$, high-density carbon $(\text{C}, \langle A\rangle/\langle Z\rangle = 2)$, and glow-discharge polymer $(\text{CH}, \langle A\rangle/\langle Z\rangle = 1.85)$. In C and Be ablators, multiple experi-

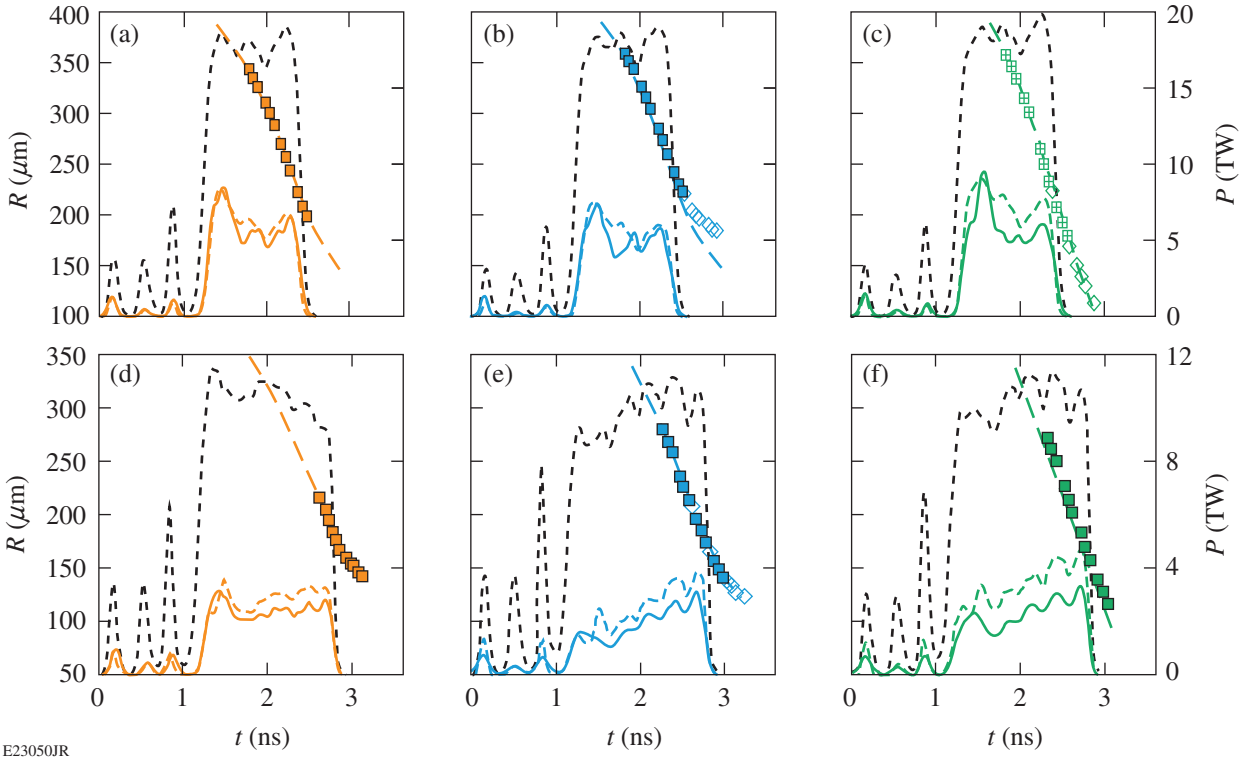

Figure 139.9
Comparison of the calculated (dashed lines) and measured (symbols) shell trajectories (the different symbols represent different shots) and of the calculated (dashed lines) and measured (solid line) scattered-light power. The results are presented for [(a),(d)] CH, [(b),(e)] C, and [(c),(f)] Be ablators at high and low laser power (black dashed lines, right axis).

ments were performed to demonstrate reproducibility of these results. The ability of the simulations to accurately reproduce both the measured trajectories and scattered powers suggests that the hydrodynamic efficiency is well modeled with *LILAC* for all three ablators at both high and low intensities.

Figures 139.10(a) and 139.10(b) show that the velocity of the shell at the end of the laser pulse is increased by 20% in the Be ablators at both low and high intensities compared to the CH ablators. Since the initial target mass was held constant, a higher velocity suggests a larger kinetic energy of the shell, but this is slightly reduced by a smaller final mass because of a higher mass-ablation rate. For the three ablators, the total laser absorption was similar at low intensity (~80%) and high intensity (~70%). This indicates that the increased velocity in Be ablators results from the transfer of the absorbed laser energy to the kinetic energy of the shell. Increasing $\langle A\rangle/\langle Z\rangle$ improves the coupling of the absorbed energy to the kinetic energy of the shell by increasing the mass density near the critical density (i.e., where the laser energy is absorbed).[22]

Figure 139.10(c) compares the ablation pressure calculated during the implosion at a similar convergence ratio of 1.5 for the three ablators at low and high laser intensities. An ~10% increase is observed for the Be ablator compared to the C and CH ablators as a result of the increased $\langle A\rangle/\langle Z\rangle$. Simulations suggest that hydro-equivalent ignition designs for OMEGA that use a Be layer can increase the ablation pressure by ~7% compared with the standard CD/DT design, allowing the IFAR to be reduced to 27 (Fig. 139.5) (Ref. 9).

3. Reduced-Beam-Size Experiments

The reduced-beam-size experiments used laser beams smoothed by PS and DPP. Fifty-seven phase plates designed to produce elliptical spots were oriented with their minor axes aligned in the direction of the wedge dispersion of the PS crystal, producing a nearly round R_b = 215-μm (95% encircled energy) laser spot at best focus. The ellipticities of these laser spots were measured to be less than 15%. Three round DPP's with a best-focus radius of R_b = 210 μm were used to complete the set. The radii of the laser spots were varied by defocusing the laser beams. A triple-picket laser pulse shape with a 1.6-ns square drive pulse and 18 kJ of total energy was used to set the shell on a low adiabat ($\alpha \approx 3$). The outer radius of the CH capsule was R_t = 430 μm, with a wall thickness of 27 μm.

Figure 139.11(a) shows the measured shell trajectories when the radius of each laser-beam spot was scaled. The smaller beam spots resulted in a higher ablation pressure, which accelerated the target significantly faster. Even for a moderate reduction in beam size $\left(R_b/R_t = 1 \text{ to } R_b/R_t = 0.9\right)$, a significant increase in velocity was observed: 186 km/s to 194 km/s (~5% increase). Good agreement between the simulated and measured shell trajectories and scattered-light powers was observed for all focal-spot radii. The improved coupling was a result of (1) more-normal rays that deposit their energy closer to the ablation surface and (2) the reduction of CBET.[13]

Figure 139.11(b) shows the ablation pressure calculated from the simulations at a convergence ratio of 1.5. A 50% increase in

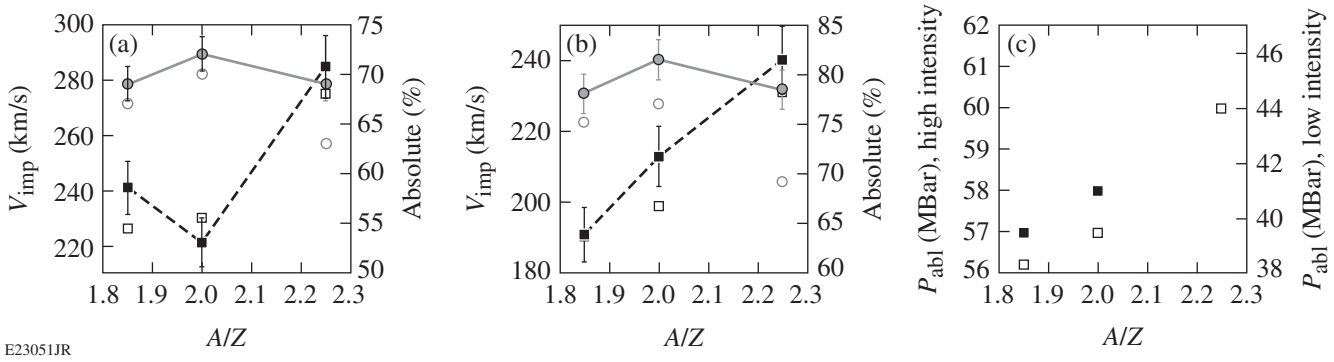

Figure 139.10
Comparison of the shell velocities measured at the end of the laser pulse (solid squares) and the total laser absorption determined from the measured scattered light (solid circles) for CH $\left(\langle A\rangle/\langle Z\rangle = 1.85\right)$, C $\left(\langle A\rangle/\langle Z\rangle = 2\right)$, and Be $\left(\langle A\rangle/\langle Z\rangle = 2.25\right)$ ablators at (a) high and (b) low laser intensities; the corresponding calculated values are shown as open symbols. (c) Comparison of the simulated ablation pressure at a convergence ratio of 1.5 for CH $\left(\langle A\rangle/\langle Z\rangle = 1.85\right)$, C $\left(\langle A\rangle/\langle Z\rangle = 2\right)$, and Be $\left(\langle A\rangle/\langle Z\rangle = 2.25\right)$ ablators at low (open squares) and high (solid squares) laser intensities.

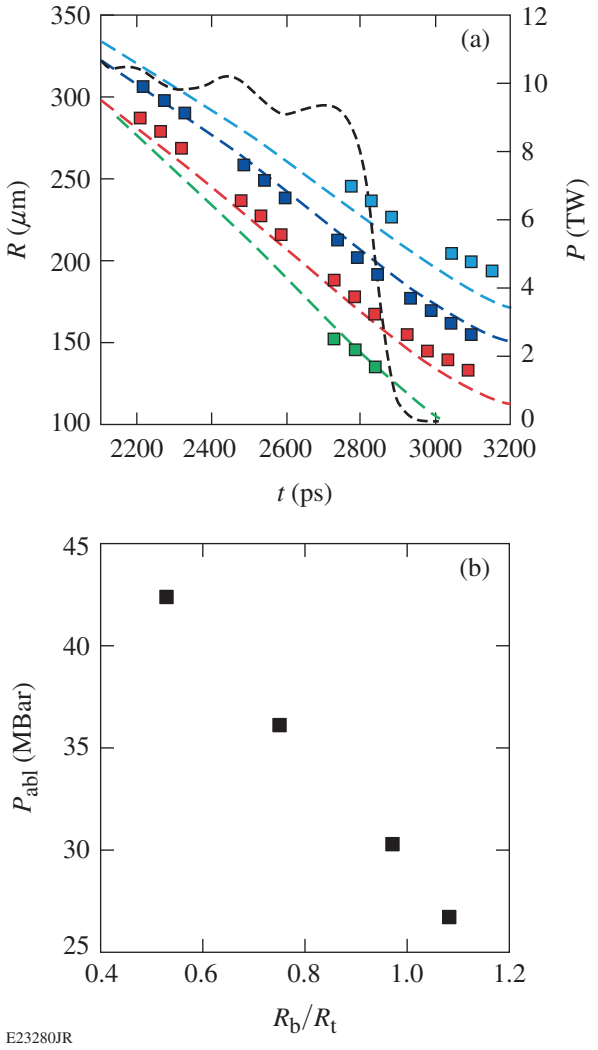

Figure 139.11
(a) Comparison of the measured (squares) and simulated (dashed lines) shell trajectories for $R_b/R_t = 0.5$ (green), $R_b/R_t = 0.9$ (red), $R_b/R_t = 1$ (blue), and $R_b/R_t = 1.1$ (light blue). A similar laser pulse was measured for each shot (black line, right axis). (b) The ablation pressure calculated at a convergence ratio of 1.5.

the ablation pressure was calculated when R_b/R_t was varied from 1.1 to 0.5.

Figure 139.12(a) shows the standard deviation in the variation of the position of the inner gradient around the image for various laser-beam diameters. When the laser-beam size is reduced, the standard deviation of the low-mode nonuniformities measured at the ablation surface increases from 1% to more than 10%. The structure of the perturbations grows at positions consistent with regions where the illumination is lower. The standard deviation of the low-mode perturbations measured from the XRFC images is compared to the standard deviation of the low-mode nonuniformity of the absorbed laser power averaged over the entire laser pulse for different R_b/R_t [Fig. 139.12(b)]. When the size of the focal spot is reduced, the illumination nonuniformity increases and the shell perturbations compromise the target compression. Simulations suggest that the laser-beam diameters can be reduced to 80% of the target diameter before significant degradation in yield is observed.[8] In this case, simulations indicate that the ablation pressure was increased by 24%, allowing for a hydro-equivalent

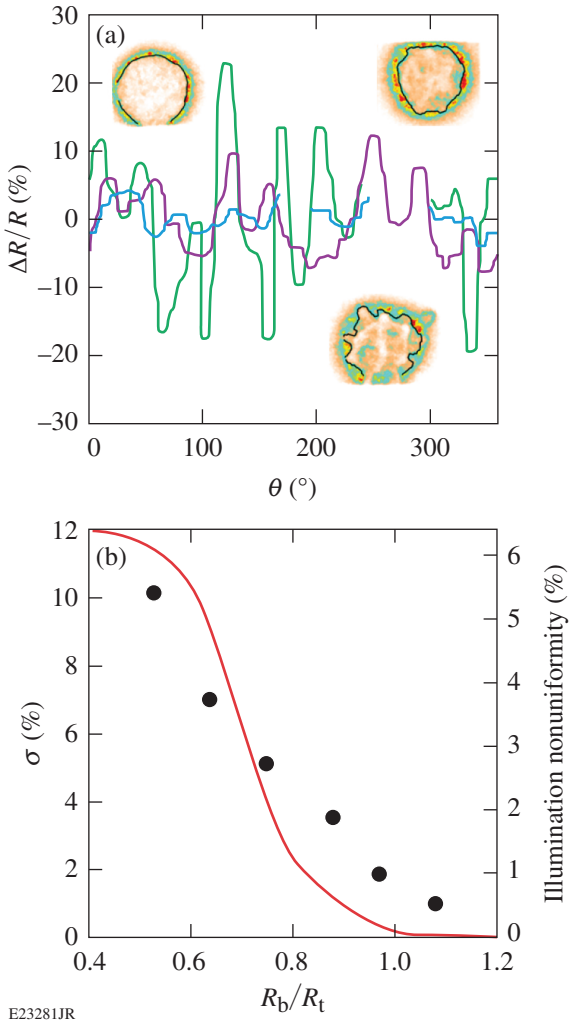

Figure 139.12
(a) Comparison of the low-mode shell perturbations measured for $R_b/R_t = 0.5$ (green line, bottom inset), $R_b/R_t = 0.75$ (purple line, top right inset), and $R_b/R_t = 1$ (blue line, top left inset) at an averaged radius of 175 μm. (b) Comparison of the standard deviation of the shell perturbation obtained in experiments (left axis) with the standard deviation of the simulated nonuniformity in the absorbed laser power averaged over the entire laser pulse (red line, right axis).

ignition design on OMEGA with an IFAR of 22—close to the current stability threshold (Fig. 139.5).

To further reduce the beam size, a two-stage zooming scheme has been proposed where large beams are used during the pickets and small beams are used during the main drive when the conduction zone is large enough to smooth low-mode laser nonuniformity.[23,24] By using $R_b/R_t = 0.6$ during the main drive, nearly all of the ablation pressure lost to CBET is recovered and a hydro-equivalent ignition design is well below the current stability threshold (Fig. 139.5).

Conclusions

Demonstrating hydro-equivalent ignition at the Omega Laser Facility is a first step toward direct-drive ignition on the NIF. Achieving hydro-equivalent ignition on OMEGA requires an implosion velocity $>3.5 \times 10^7$ cm/s, an areal density >300 mg/cm^2, and a hot-spot pressure above 100 Gbar. Currently, the best-performing implosions, which are driven to ignition-relevant velocities, do not reach hydro-equivalent areal densities, limiting the peak hot-spot pressure to ~40 Gbar (Ref. 9). One approach to recovering the hydro-equivalent areal density is to decrease the IFAR by using thicker shells. To drive the thicker shells to the relevant velocities, the hydrodynamic efficiency must be improved.

In this article, the hydrodynamic efficiency has been studied in three different direct-drive experiments. The coupling of the laser energy to the plasma (absorption) was determined by measuring the scattered-light power. The plasma energy transferred to the kinetic energy of the shell was studied by measuring the shell trajectory, the shell velocity, and the neutron burn history. These experimental observables were compared with 1-D hydrodynamic simulations (conducted by the code *LILAC*) that include CBET and nonlocal thermal-transport models. In each case, excellent agreement was observed, suggesting that the code was able to reproduce the hydrodynamic parameters of the imploding shell. For Be targets, the ablation pressure of the laser was shown to increase by ~10% compared with the C and standard CH ablators. When the spot size of the laser was reduced by ~50%, the ablation pressure was shown to increase by a factor of 1.6, but the increased illumination nonuniformity compromised the integrated target performance. In future experiments, three new designs will be tested: multilayer ablators,[9] beam diameters that are 80% of the target diameter, and two-stage zooming. Simulations indicate that the ablation pressure in hydro-equivalent designs will be increased by 7% for the first case, 24% for the second case, and 50% for the third case.

ACKNOWLEDGMENT

This material is based upon work supported by the Department of Energy National Nuclear Security Administration under Award Number DE-NA0001944, the University of Rochester, and the New York State Energy Research and Development Authority. The support of DOE does not constitute an endorsement by DOE of the views expressed in this article.

REFERENCES

1. J. Nuckolls *et al*., Nature **239**, 139 (1972).
2. T. R. Boehly, D. L. Brown, R. S. Craxton, R. L. Keck, J. P. Knauer, J. H. Kelly, T. J. Kessler, S. A. Kumpan, S. J. Loucks, S. A. Letzring, F. J. Marshall, R. L. McCrory, S. F. B. Morse, W. Seka, J. M. Soures, and C. P. Verdon, Opt. Commun. **133**, 495 (1997).
3. J. Paisner *et al*., Laser Focus World **30**, 75 (1994).
4. R. Nora, R. Betti, K. S. Anderson, A. Shvydky, A. Bose, K. M. Woo, A. R. Christopherson, J. A. Marozas, T. J. B. Collins, P. B. Radha, S. X. Hu, R. Epstein, F. J. Marshall, R. L. McCrory, T. C. Sangster, and D. D. Meyerhofer, Phys. Plasmas **21**, 056316 (2014).
5. J. Delettrez, Can. J. Phys. **64**, 932 (1986).
6. V. N. Goncharov, T. C. Sangster, P. B. Radha, R. Betti, T. R. Boehly, T. J. B. Collins, R. S. Craxton, J. A. Delettrez, R. Epstein, V. Yu. Glebov, S. X. Hu, I. V. Igumenshchev, J. P. Knauer, S. J. Loucks, J. A. Marozas, F. J. Marshall, R. L. McCrory, P. W. McKenty, D. D. Meyerhofer, S. P. Regan, W. Seka, S. Skupsky, V. A. Smalyuk, J. M. Soures, C. Stoeckl, D. Shvarts, J. A. Frenje, R. D. Petrasso, C. K. Li, F. Séguin, W. Manheimer, and D. G. Colombant, Phys. Plasmas **15**, 056310 (2008).
7. P. Michel, L. Divol, E. A. Williams, S. Weber, C. A. Thomas, D. A. Callahan, S. W. Haan, J. D. Salmonson, S. Dixit, D. E. Hinkel, M. J. Edwards, B. J. MacGowan, J. D. Lindl, S. H. Glenzer, and L. J. Suter, Phys. Rev. Lett. **102**, 025004 (2009).
8. I. V. Igumenshchev, W. Seka, D. H. Edgell, D. T. Michel, D. H. Froula, V. N. Goncharov, R. S. Craxton, L. Divol, R. Epstein, R. Follett, J. H. Kelly, T. Z. Kosc, A. V. Maximov, R. L. McCrory, D. D. Meyerhofer, P. Michel, J. F. Myatt, T. C. Sangster, A. Shvydky, S. Skupsky, and C. Stoeckl, Phys. Plasmas **19**, 056314 (2012).
9. V. N. Goncharov, T. C. Sangster, R. Betti, T. R. Boehly, M. J. Bonino, T. J. B. Collins, R. S. Craxton, J. A. Delettrez, D. H. Edgell, R. Epstein, R. K. Follet, C. J. Forrest, D. H. Froula, V. Yu. Glebov, D. R. Harding, R. J. Henchen, S. X. Hu, I. V. Igumenshchev, R. Janezic, J. H. Kelly, T. J. Kessler, T. Z. Kosc, S. J. Loucks, J. A. Marozas, F. J. Marshall, A. V. Maximov, R. L. McCrory, P. W. McKenty, D. D. Meyerhofer, D. T. Michel, J. F. Myatt, R. Nora, P. B. Radha, S. P. Regan, W. Seka, W. T. Shmayda, R. W. Short, A. Shvydky, S. Skupsky, C. Stoeckl, B. Yaakobi, J. A. Frenje, M. Gatu-Johnson, R. D. Petrasso, and D. T. Casey, Phys. Plasmas **21**, 056315 (2014).
10. P. B. Radha, C. Stoeckl, V. N. Goncharov, J. A. Delettrez, D. H. Edgell, J. A. Frenje, I. V. Igumenshchev, J. P. Knauer, J. A. Marozas, R. L. McCrory, D. D. Meyerhofer, R. D. Petrasso, S. P. Regan, T. C. Sangster, W. Seka, and S. Skupsky, Phys. Plasmas **18**, 012705 (2011).
11. T. C. Sangster, V. N. Goncharov, R. Betti, P. B. Radha, T. R. Boehly, D. T. Casey, T. J. B. Collins, R. S. Craxton, J. A. Delettrez, D. H.

Edgell, R. Epstein, C. J. Forrest, J. A. Frenje, D. H. Froula, M. Gatu-Johnson, V. Yu. Glebov, D. R. Harding, M. Hohenberger, S. X. Hu, I. V. Igumenshchev, R. Janezic, J. H. Kelly, T. J. Kessler, C. Kingsley, T. Z. Kosc, J. P. Knauer, S. J. Loucks, J. A. Marozas, F. J. Marshall, A. V. Maximov, R. L. McCrory, P. W. McKenty, D. D. Meyerhofer, D. T. Michel, J. F. Myatt, R. D. Petrasso, S. P. Regan, W. Seka, W. T. Shmayda, R. W. Short, A. Shvydky, S. Skupsky, J. M. Soures, C. Stoeckl, W. Theobald, V. Versteeg, B. Yaakobi, and J. D. Zuegel, Phys. Plasmas **20**, 056317 (2013).

12. D. T. Michel, V. N. Goncharov, I. V. Igumenshchev, R. Epstein, and D. H. Froula, Phys. Rev. Lett. **111**, 245005 (2013).

13. D. H. Froula, I. V. Igumenshchev, D. T. Michel, D. H. Edgell, R. Follett, V. Yu. Glebov, V. N. Goncharov, J. Kwiatkowski, F. J. Marshall, P. B. Radha, W. Seka, C. Sorce, S. Stagnitto, C. Stoeckl, and T. C. Sangster, Phys. Rev. Lett. **108**, 125003 (2012).

14. J. J. MacFarlane *et al*., High Energy Density Phys. **3**, 181 (2007).

15. T. R. Boehly, V. A. Smalyuk, D. D. Meyerhofer, J. P. Knauer, D. K. Bradley, R. S. Craxton, M. J. Guardalben, S. Skupsky, and T. J. Kessler, J. Appl. Phys. **85**, 3444 (1999).

16. S. Skupsky, R. W. Short, T. Kessler, R. S. Craxton, S. Letzring, and J. M. Soures, J. Appl. Phys. **66**, 3456 (1989).

17. T. J. Kessler, Y. Lin, J. J. Armstrong, and B. Velazquez, in *Laser Coherence Control: Technology and Applications*, edited by H. T. Powell and T. J. Kessler (SPIE, Bellingham, WA, 1993), Vol. 1870, pp. 95–104.

18. V. N. Goncharov, T. C. Sangster, T. R. Boehly, S. X. Hu, I. V. Igumenshchev, F. J. Marshall, R. L. McCrory, D. D. Meyerhofer, P. B. Radha, W. Seka, S. Skupsky, C. Stoeckl, D. T. Casey, J. A. Frenje, and R. D. Petrasso, Phys. Rev. Lett. **104**, 165001 (2010).

19. D. T. Michel, C. Sorce, R. Epstein, N. Whiting, I. V. Igumenshchev, R. Jungquist, and D. H. Froula, Rev. Sci. Instrum. **83**, 10E530 (2012).

20. D. K. Bradley *et al*., Rev. Sci. Instrum. **66**, 716 (1995).

21. A. K. Davis, D. T. Michel, S. X. Hu, R. S. Craxton, R. Epstein, V. N. Goncharov, I. V. Igumenshchev, T. C. Sangster, and D. H. Froula, Rev. Sci. Instrum. **85**, 11D616 (2014).

22. W. M. Manheimer, D. G. Colombant, and J. H. Gardner, Phys. Fluids **25**, 1644 (1982).

23. D. H. Froula, T. J. Kessler, I. V. Igumenshchev, R. Betti, V. N. Goncharov, H. Huang, S. X. Hu, E. Hill, J. H. Kelly, D. D. Meyerhofer, A. Shvydky, and J. D. Zuegel, Phys. Plasmas **20**, 082704 (2013).

24. I. V. Igumenshchev, D. H. Froula, D. H. Edgell, V. N. Goncharov, T. J. Kessler, F. J. Marshall, R. L. McCrory, P. W. McKenty, D. D. Meyerhofer, D. T. Michel, T. C. Sangster, W. Seka, and S. Skupsky, Phys. Rev. Lett. **110**, 145001 (2013).